Building without the architect: the dispensable role of MICOS in *de novo* cristae formation in malaria parasites

Silvia Tassan-Lugrezin[1*], Irina Bregy[2*], Judith López Orra[1], Nicholas I. Proellochs[1], Geert-Jan van Gemert[1], Rianne Stoter[1], Felix Evers[1], Taco W.A. Kooij[1+], Laura van Niftrik[2+]

[1]Department of Medical Microbiology, Radboud University Medical Centre, Nijmegen, The Netherlands

[2] Department of Microbiology, Faculty of Science, Radboud University, Nijmegen, The Netherlands

[*] These authors equally contributed to the manuscript

[+] Corresponding authors, contributed equally to the manuscript

Summary

The malaria parasite mitochondria represent the only tractable, naturally occurring system in which cristae, the characteristic invaginations of the inner mitochondrial membrane, are known to be formed *de novo*. In traditional model organisms, the central complex involved in cristae organization is the mitochondrial contact site and cristae organizing system (MICOS). However, whether MICOS has an active role in the initial formation of cristae remained unclear. We identified two putative *Plasmodium falciparum* MICOS components, *Pf*MIC19 and *Pf*MIC60 and show that both genes are dispensable in asexual blood stages, gametocytes, and mosquito stages, albeit with a mild reduction in oocyst numbers. Immunofluorescence microscopy and electron tomography of gametocytes lacking either or both MICOS orthologues showed aberrant mitochondrial morphology and abnormal cristae, with a marked reduction of crista junctions. Thus, by utilizing the unique properties of *P. falciparum*, we confirmed the involvement of *Pf*MIC19 and *Pf*MIC60 in the organization of crista junctions, while providing evidence that MICOS is not required for the formation of cristae.

Keywords: *Plasmodium falciparum*, malaria, mitochondria, cristae, MICOS, MIC60, MIC19

Introduction

The mitochondrion is a double membrane-bound organelle found in most eukaryotes. Its primary function is to generate ATP through oxidative phosphorylation. The mitochondrion bears an outer mitochondrial membrane (OMM), which is a selectively permeable barrier to the cytoplasm, and an inner mitochondrial membrane (IMM), which separates the mitochondrial matrix from the intermembrane space. The IMM is divided into two distinct domains: the cristae membrane and the inner boundary membrane. The cristae membrane is highly convoluted and rich in ATP synthase and the electron transport chain complexes thus

39 forming a specialized area responsible for oxidative phosphorylation. The inner boundary
40 membrane hosts proteins and protein complexes responsible for exchange of metabolites,
41 protein translocation, and mitochondrial fusion (1-3). Both membranes are connected at the
42 crista junctions. Crista junctions are known to be organized by a multi-subunit protein
43 complex, the mitochondrial contact site and cristae organizing system (MICOS) (3-6).
44 Together with proteins of the OMM, MICOS is also part of the mitochondrial intermembrane
45 space bridging complex that mediates contacts between the IMM and OMM (7-9). In humans,
46 MICOS is organized into two protein sub-complexes integrated in the cristae membrane, the
47 MIC10 and MIC60 sub-complexes, consisting of four and three different components,
48 respectively (9-11). MIC60 is one of the key components of MICOS implicated in generating
49 the negative curvature at the base of the cristae membrane (12, 13). MIC60 consists of an N-
50 terminal transmembrane domain, responsible for anchoring it to the IMM, a coiled-coil
51 domain and a mitofilin domain at the C-terminal end of the protein. These two C-terminal
52 domains are essential to form and stabilize crista junctions through the tetramerization of
53 MIC60 (13-15).
54
55 Strikingly, the mitochondrion of *Plasmodium falciparum,* the most virulent causing agent of
56 human malaria, departs from the canonical model of mitochondria. Asexual blood-stage
57 parasites (ABS) have a single acristate mitochondrion that harbours very little respiratory
58 chain complex components (16). During development to the sexual, mosquito transmissible
59 stages, also called gametocytes, the single mitochondrion separates into a set of 4-8
60 mitochondria (17) in which canonical mitochondrial processes, such as tricarboxylic acid cycle
61 and oxidative phosphorylation gain relevance (16, 18-20). This is accompanied by a large
62 increase in expression of ATP synthase and all relevant electron transport chain complexes
63 but also by the *de novo* emergence of bulbous cristae in the mitochondria (16, 17).
64
65 Even though mutation-induced aberrations of mitochondrial cristae morphology in *P.*
66 *falciparum* have been sporadically reported (21), details on the molecular underpinnings of
67 the bulbous shape and *de novo* biogenesis of cristae in *P. falciparum* gametocytes remain
68 largely unknown. While a recent study in a related apicomplexan parasite, *Toxoplasma gondii*,
69 has shown that the bulbous morphology is associated with highly divergent and large ATP
70 synthase assemblies (22), the mechanisms involved in forming and maintaining stable crista
71 junctions have yet to be investigated. Very little is known about any MICOS-like complex
72 components or their potential roles in governing membrane architecture at the crista junction
73 (21). Prior research has suggested PF3D7_1007800 as a putative orthologue of *MIC60* in *P.*
74 *falciparum* (*PfMIC60*) based on sequence homology to the characteristic mitofilin domain, but
75 until now, no other subunits of MICOS have been identified in *P. falciparum* despite a high
76 degree of conservation in other cristate eukaryotes (9, 23). It is noteworthy that even though
77 sequence homology and composition of MICOS diverges between clades, overall architecture
78 is comparable to the opisthokont models. Irrespective of the shape of an organism's cristae,

79 the crista junctions have been described as tubular channels that connect the cristae
80 membrane to the inner boundary membrane (22, 24).
81
82 Although MICOS has mainly been described as an organizer of crista junctions, conclusive
83 evidence about its involvement in the initial formation of cristae is still lacking. In this study,
84 we used a combination of experimental genetics, high-resolution fluorescence microscopy,
85 electron microscopy and electron tomography to elucidate the involvement of the parasite's
86 MICOS in cristae organization, with clear distinction from cristae formation.
87

88 # Results

89 ## Identification of putative *Pf*MICOS components

90
91 To further investigate previously reported sequence homology of the MIC60 mitofilin domain
92 to the *Pf*MIC60 candidate PF3D7_1007800 (9), we compared publicly available AlphaFold
93 predictions of the protein sequence of the canonical MIC60 and our candidate sequence
94 (Figure 1A, C and Figure S1A, C). In addition to the putative mitofilin domain in *Pf*MIC60, we
95 identified a putative lipid binding domain and a coiled coil domain of similar length as
96 described for opisthokonts MIC60. Interestingly, *Pf*MIC60 is much larger than the human
97 MICOS counterpart, with a large, poorly predicted N-terminal extension. The only domain
98 detected in this region of the predicted molecule is an antiparallel array of ten β-sheets of
99 unknown function. Since the *P. falciparum* genome lacks obvious orthologues of additional
100 MICOS components, we re-examined our publicly available gametocyte-derived complexome
101 profiling datasets (16). *Pf*MIC60 did not enter standard mass range gels (16) but in samples
102 separated on specialized, high molecular mass gels, we found *Pf*MIC60 consistently
103 comigrates with PF3D7_1108800 at an apparent mass of 4-5 MDa (Figure 1E, Supp.
104 Information 1). PF3D7_1108800 is conserved across the *Plasmodium* genus (OG7_0323199)
105 (25) and, while it lacks clear sequence homology outside of that, the AlphaFold prediction
106 features a conserved CC-helix-CC-helix (CHCH) domain also found in MIC19, a known
107 interactor of MIC60 in opisthokonts (Figure 1B, D). Based on this structural similarity and
108 comigration pattern, we propose to provisionally designate PF3D7_1108800 as *Pf*MIC19.
109

110 ## *Pf*MIC60 and *Pf*MIC19 are expressed during gametocyte stages.

111 To study the function of *Pf*MIC19 and *Pf*MIC60 as possible MICOS components, we analysed
112 their expression profile and localization in ABS and gametocytes. Therefore, we generated
113 two transgenic parasite lines, *mic19-HA* and *mic60-HA* in which we introduced a *3xHA-GlmS*
114 tag at the 3' end of the respective genes. The transgenic lines also contain a mitochondrially
115 targeted mScarlet for visualization of the organelle and protein co-localization (Figure S2A).
116 Correct integration and absence of wild-type (WT) parasites was confirmed through
117 diagnostic PCR (Figure S2B). Western blot analysis of mixed ABS and mature gametocyte
118 samples revealed that *Pf*MIC19 (19.7 kDa) and *Pf*MIC60 (120 kDa) are absent in acristate ABS

119 but expressed in the cristate sexual blood stages (Figure 1F). As a positive control for
120 mitochondrial localization, we used the previously published MitoRed line (26), which
121 expresses the mitochondrially targeted mScarlet from a silent intergenic locus. Unfortunately,
122 attempts to localise *Pf*MIC19-HA and *Pf*MIC60-HA using conventional immunofluorescence
123 microscopy and ultra-expansion microscopy were unsuccessful, likely due to their naturally
124 low abundance (Figure S2C-D) highlight by our western blot analysis (Figure 1F).
125

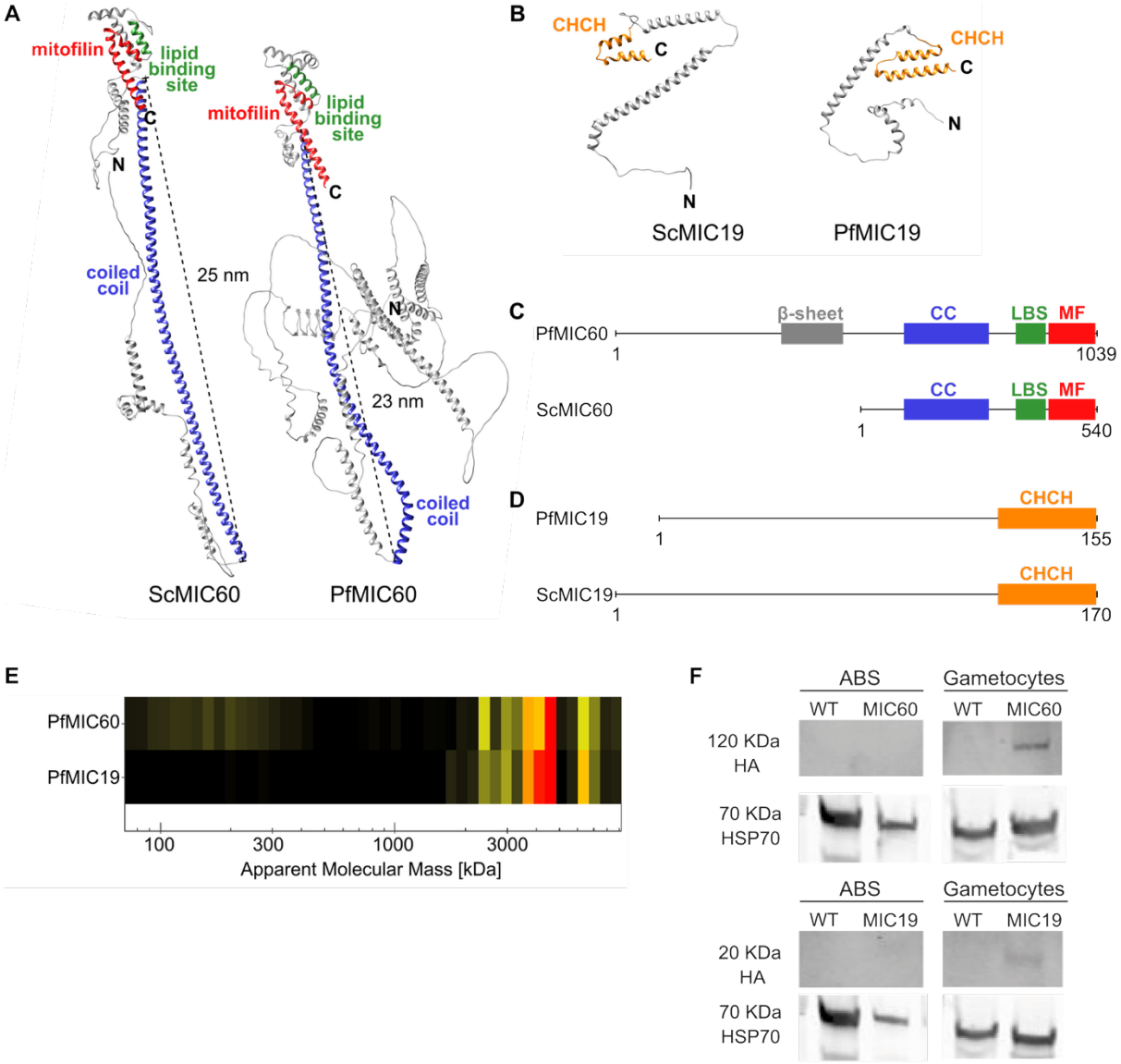

126
127 ***Figure 1. Identification of PfMICOS candidates based on predictive structural similarities,***
128 ***complexome profiling and the characteristic expression patterns expected for cristae modulators****. A)*
129 *AlphaFold predictions of ScMIC60 (Saccharomyces cerevisiae) and PfMIC60 (27, 28). TED consensus*
130 *domain predicted mitofilin domain (red), lipid binding site (green) and coiled coil domain (blue,*
131 *theoretical length annotated) are highlighted (29). N- and C-terminus are annotated. (local pLDDT*
132 *confidence information in Figure S1). B) AlphaFold predictions of ScMIC19 and PfMIC19 (27, 28). TED*
133 *predicted CC-helix-CC-helix (CHCH) domain is highlighted (29). N- and C-terminus are annotated. (local*
134 *pLDDT confidence information in Figure S1). C) Schematic overview of the TED predicted domain*
135 *architecture of ScMIC60 and PfMIC60. The additional domain annotated for PfMIC60 consists of ten*

136 *antiparallel β-sheets of unknown function. D) Schematic overview of the TED predicted domain*
137 *architecture of ScMIC19 and PfMIC19. E) Heat maps showing co-migration of PfMIC19 with PfMIC60.*
138 *F) Western blot analysis of ABS and mature gametocytes of MIC19-HA and MIC60-HA. Tagged proteins*
139 *were detected with rat anti-HA (PfMIC19 and PfMIC60, top) and rabbit anti-HSP70 was used as a*
140 *loading control (bottom).*

141 **_Pf_MIC19 and _Pf_MIC60 are not essential for _P. falciparum in vitro_ life-cycle progression**

142 To investigate the essentiality of *Pf*MIC19 and *Pf*MIC60 during the *P. falciparum* life cycle, we
143 generated the knockout parasite lines *mic19*⁻ and *mic60*⁻ in which the respective genes were
144 replaced by a cytoplasmic green fluorescent protein (GFP) (Figure S2A). In addition, we
145 generated the *mic19/60*⁻ double-knockout line in which *PfMIC60* was replaced by a
146 cytoplasmic mCherry in the *mic19*⁻ genetic background (Figure S3A). Diagnostic PCR
147 confirmed proper integration and absence of WT parasites in all the generated lines (Figure
148 S2B and Figure S3B). To assess parasite viability, we performed a standard growth assay on
149 ABS parasites. Parasite replication was followed for two replication cycles, revealing that ABS
150 of *mic19*⁻, *mic60*⁻, and *mic19/60*⁻ grow at a comparable rate to parental parasites (NF54)
151 (Figure 2A). Interestingly, *mic19*⁻, *mic60*⁻, and *mic19/60*⁻ also produced mature gametocytes
152 with no apparent delay. To verify their viability, we performed exflagellation assays that
153 revealed no difference in maturation compared to the NF54 parental control (Figure 2B). In
154 addition, gametocytes were fed to mosquitoes through standard membrane feeding assays.
155 All lines infected mosquitoes and we observed a reduction in infection rate as well as oocyst
156 numbers in *mic19*⁻, *mic60*⁻, and *mic19/60*⁻ compared to NF54, with the transmission
157 reduction of 77% (95% CI: 69, 83) for *mic19*⁻, 52% (95% CI: 39, 62) for *mic60*⁻, and 47% (95%
158 CI: 30, 59) for *mic19/60*⁻. (Figure 2C and Figure 2D). Nevertheless, sporozoite production was
159 confirmed for all generated knockout lines, indicating that *Pf*MIC19 and *Pf*MIC60 are not
160 essential for the parasites to complete the mosquito stage development (Figure S5). In
161 summary, under *in vitro* culture conditions, *Pf*MIC19 and *Pf*MIC60 are dispensable for survival
162 and development of ABS and gametocytes. Absence of these MICOS components is also
163 compatible with progression through mosquito stage development albeit at a reduced rate.
164

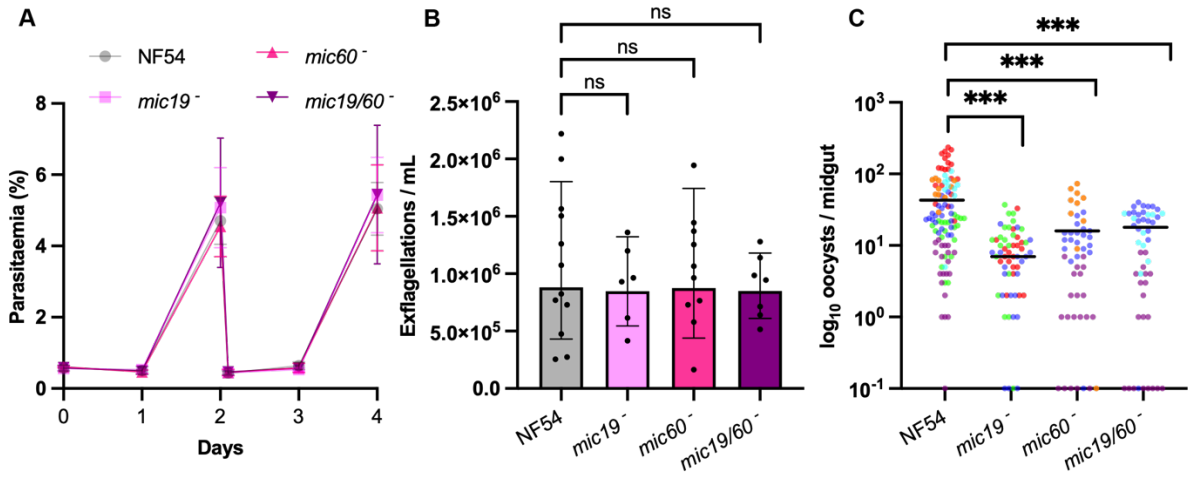

D

Exp n°	NF54		*mic19* -		*mic60* -		*mic19/60* -	
	% inf mosq.	mean	% inf mosq.	mean	% inf mosq.	mean	% inf mosq.	mean
Exp1	100% (20/20)	120,3	100% (20/20)	8,9				
Exp2	100% (20/20)	16,1	95% (19/20)	13,2				
Exp3	100% (20/20)	27,3	85% (17/20)	5,8	95% (19/20)	13,2	95% (19/20)	25,2
Exp4	100% (10/10)	63,9			90% (9/10)	37,6		
Exp5	95% (19/20)	5,7			80% (16/20)	2,25	60% (12/20)	2,2
Exp6	100% (10/10)	68					100% (10/10)	18

***Figure 2. Consequences of deletion of Pf*MIC60 *and Pf*MIC19 *on differentiation and survival of* P. falciparum.** *A) Growth curve of NF54, mic19⁻, mic60⁻, and mic19/60⁻ ABS over time (in days). (n =3 for NF54, mic19⁻, mic60⁻ and n=2 for mic19/60⁻). B) Exflagellation assay of NF54, mic19⁻, mic60⁻, and mic19/60⁻. (n >=6). C) Infection of A. stephensi mosquitoes with NF54, mic19⁻, mic60⁻, and mic19/60⁻ in 6 independent experiments indicated in different colours. Means (black line): NF54 = 43, mic19⁻ = 7.0, mic60⁻ = 15.0 and mic19/60⁻ = 17.1. Statistical significance is indicated as follows: ns ≥ 0.05, *p < 0.05, **p < 0.01, ***p < 0.001, ****p < 0.0001 D). Summary of infected mosquitoes and mean oocyst count per midgut in every independent experiment displayed in C.*

Knockout of *PfMIC60* and *PfMIC19* impairs mitochondrial morphology in gametocytes

Next, we investigated the impact of *Pf*MIC19 and *Pf*MIC60 absence on mitochondrial morphology. Due to the lack of detectable protein expression in ABS, we focused on mature gametocytes, where cristae are abundant and protein expression was detected in western blot. We stained mitochondria of parental NF54 line, single and double knockout line mature gametocytes with MitoTracker and used tubulin as a male marker (30). To analyse the variability of normal mitochondrial morphology in the NF54 background, we quantified the imaging data using the Mitochondria-Analyzer plug-in for Fiji (31, 32). Mitochondria were classified into three categories: (1) tubular, when only one/two elongated and highly branched mitochondrial signals were identified per cell body; (2) intermediate, when multiple partially branched mitochondrial signals were observed; and (3) rounded-up, when mitochondria appeared smaller, more spherical, and dispersed (Figure 3A). Note that light microscopy does not resolve individual mitochondria if they are in close contact with each

188 other (17). Nevertheless, the analysis revealed that mitochondrial morphology of both male
189 and female gametocytes was partially altered in all knockout lines, characterized by a
190 predominance of rounded-up and intermediate mitochondria, and a marked reduction of
191 tubular networks. (Figure 3B, Figure S6). The number of individually identifiable mitochondrial
192 intensities was 24%, 21%, and 23% higher in *mic19*$^{-}$, *mic60*$^{-}$, and *mic19/60*$^{-}$, respectively,
193 possibly indicating an increased dispersion of mitochondria throughout the cell body (Figure
194 3C). These single mitochondrial intensities were ~30% smaller (Figure 3D), more spherical
195 (36%, 24%, and 20%) (Figure 3E), and less branched (50%, 55%, and 40%) (Figure 3F) compared
196 to the parental NF54 line. In addition, total mitochondrial volume per cell was reduced in all
197 knockout lines with 15%, 17%, and 13%, respectively (Figure 3G). Interestingly, deletion of
198 both genes did not exacerbate the mitochondrial phenotype compared to the single
199 knockouts. In conclusion, while NF54 cells contain mainly tubular mitochondria, *mic19*$^{-}$,
200 *mic60*$^{-}$, and *mic19/60*$^{-}$ gametocytes have more intermediate and rounded-up mitochondria.
201

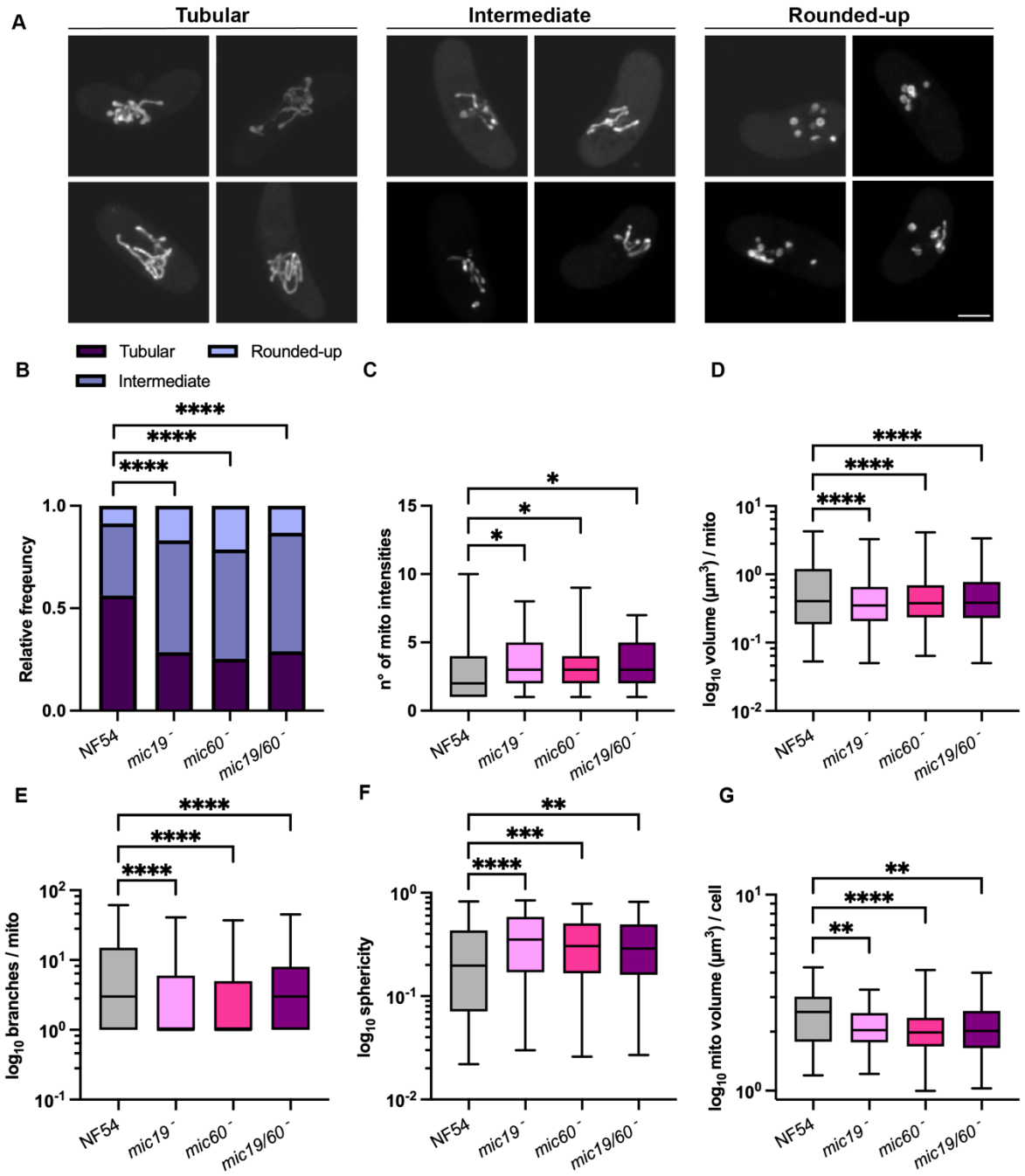

Figure 3. Fluorescence microscopy reveals aberrant mitochondrial morphology in mature* P. falciparum *mic19⁻, mic60⁻, and mic19/60⁻ gametocytes. *A) Representative fluorescent microscopy images of mature NF54 gametocytes possessing tubular, intermediate, or rounded-up mitochondria. Samples were stained with MitoTracker. Images are maximum intensity projections of Z-stack confocal Airyscan images. Scale bars: 2 µm. B) Analysis of mitochondrial shape based on mean branch length per cell. Rounded-up = branch length < 2 µm, intermediate = branch length between 2 µm and 10 µm, tubular = branch length > 10 µm. C- G) Quantification of (C) n° of detected mitochondrial intensities per cell, (D) volume per mitochondria (log), (E) branches per mitochondrion (log), (F) sphericity of mitochondria (log), (G) mitochondrial volume per cell (log). In all cases n > 3 with total number of cells >= 75. G) Statistical significance is indicated as follows: ns ≥ 0.05, *p < 0.05, **p < 0.01, ***p < 0.001, ****p < 0.0001.*

216

217 ## *Pf*MIC60 and *Pf*MIC19 are involved in shaping mitochondrial cristae

218 To assess the role of *Pf*MIC19 and *Pf*MIC60 in cristae morphology, we performed transmission
219 electron microscopy (TEM) on mature gametocyte samples of *mic19*$^{-}$, *mic60*$^{-}$, *mic19/60*$^{-}$, and
220 the parental NF54. Two-dimensional analysis of thin sections revealed cristae deformations
221 in all knockout lines (Figure 4A). We did not observe differences in cristae morphology
222 between male and female parasites. Length, width, and area occupied by individual cristae
223 from over 30 mitochondrial cross-sections per sample were measured (Figure 4B-D). Cristae
224 in *mic19*$^{-}$ gametocytes appeared wider, whereas the cristae in *mic60*$^{-}$ and *mic19/60*$^{-}$
225 gametocytes were longer, but not wider, when compared to the parental NF54. The
226 measured effect on crista length was particularly pronounced in *mic19/60*$^{-}$ with a mean crista
227 length of 155 nm compared to 96 nm for NF54 (Figure 4B). As a consequence of the increased
228 measured crista length and width in the knockout lines, crista area increased in all knockout
229 lines (Figure 4D). We expect this effect to translate into the third dimension and thus conclude
230 that the mean crista volume increases with the loss of either *PfMIC19*, *PfMIC60*, or both. Even
231 though the deletion of *PfMIC19* and/or *PfMIC60* clearly affected cristae morphology, mean
232 cristae coverage per mitochondrial cross-section remained stable across all cell lines (Figure
233 4E). The reason for the lack of a significant change in cristae coverage despite the increased
234 area per crista can be calculated from the same datapoints and shows that the mean number
235 of crista cross-sections per μm^2 of mitochondrial cross-section drops from 33.8 crista-sections
236 per μm^2 in NF54 to 20.3, 16.3 and 26.4 in *mic19*$^{-}$, *mic60*$^{-}$ and *mic19/60*$^{-}$, respectively. The
237 increased variability in cristae coverage in *mic19/60*$^{-}$ is a result of the extreme phenotypes
238 observed in some severely affected mitochondria (Figure 4F and Figure S7). We observed
239 instances of extremely long cristae, as well as mitochondria with large single- or double-
240 membraned circles within the mitochondrial cross-section. Given the observed aberrations in
241 cristae morphology in knockout lines, we conclude that membrane invaginations can still form,
242 even in the absence of *Pf*MIC19 and *Pf*MIC60, suggesting that these proteins are not essential
243 for initiating cristae formation. Nevertheless, *Pf*MIC60 and *Pf*MIC19 both play an essential
244 role in shaping nascent cristae. Furthermore, our data indicates the effect size increases with
245 simultaneous ablation of both proteins.

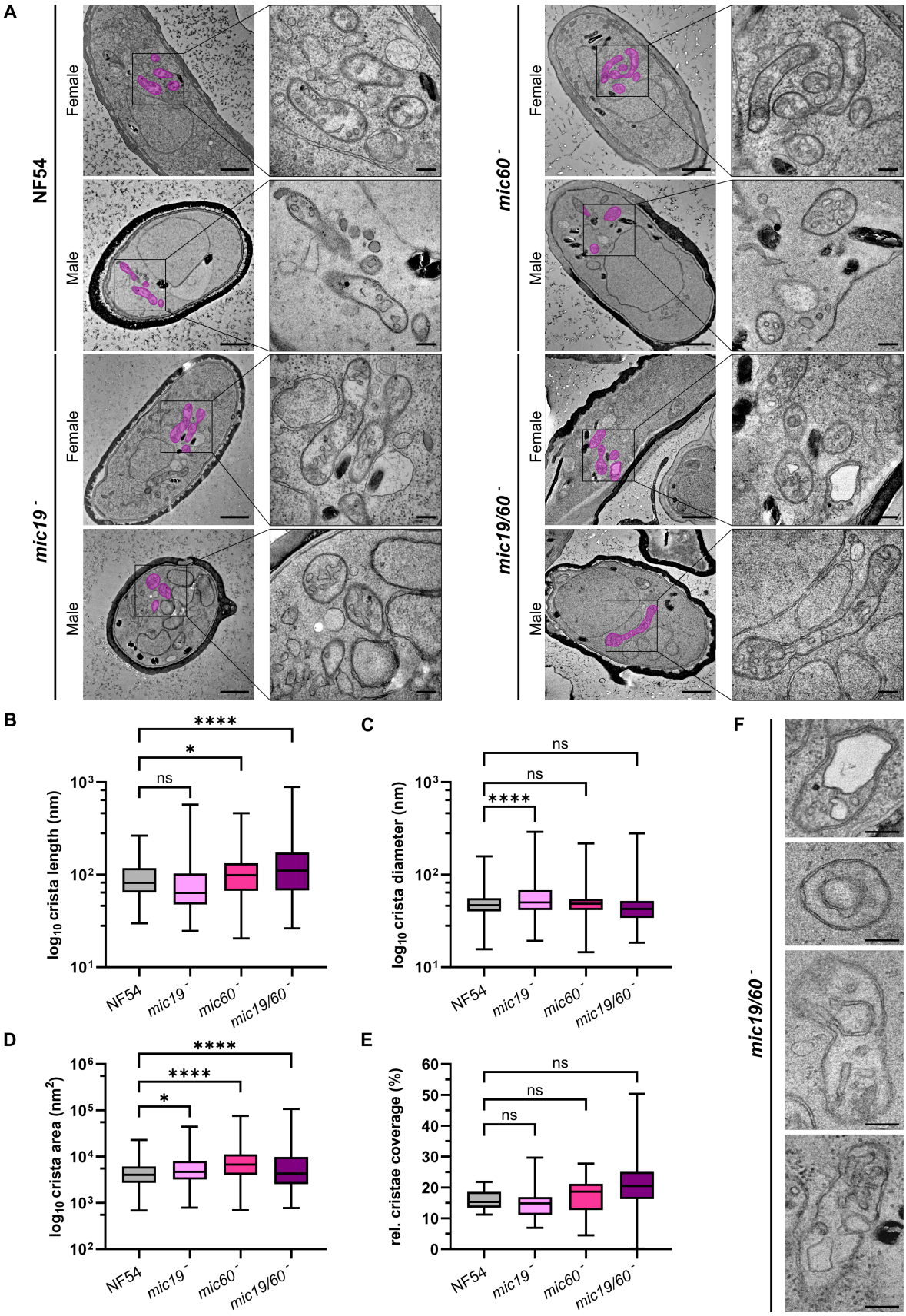

Figure 4. Transmission electron microscopy reveals aberrant cristae structures in mature* P. falciparum *mic19⁻, mic60⁻, and mic19/60⁻ gametocytes. *A) Representative micrographs of NF54 (WT), mic19⁻, mic60⁻, and mic19/60⁻ gametocytes. Mitochondria within a rectangular selection are highlighted in pink. Zoom-ins on these selections are shown on the right side of each micrograph. For*

251 *each cell line, a male and a female parasite are shown. Scale bars: 1 µm / 200 nm. B - D) Quantification*
252 *of the length (log) (B), width (log) (C), and area (log) (D) of cross-sections through individual cristae (n*
253 *≥ 100). E) Quantification of cristae coverage based on the total cristae area of a mitochondrial cross*
254 *section relative to the area of the respective mitochondrial cross section (n ≥ 30). F) Examples of*
255 *severely aberrant mitochondria as observed in TEM of mic19/60⁻ gametocytes. Scale bars: 200 nm.*
256 *Statistical significance in B – E is indicated as follows: ns ≥ 0.05, *p < 0.05, **p < 0.01, ***p < 0.001,*
257 *****p < 0.0001.*

258 ## ***Pf*MIC60 and *Pf*MIC19 are important for proper crista junction formation**

259 To delve deeper into the effects of *PfMIC19* and *PfMIC60* deletions, we performed dual-tilt
260 TEM tomography on 250 nm sections of the same samples used in Figure 4. The phenotypes
261 matched our observations from two-dimensional acquisitions. We found cristae morphology
262 to be altered in all knockout lines, with most severe aberrations found in *mic19/60⁻* (Figure
263 5A-B). We manually segmented one representative mitochondrion per parasite line to
264 visualize the observed effects (Figure 5C and Movies 1-4). We observed that in all knockout
265 parasites, we rarely identified connections between cristae membranes and the boundary
266 membrane. To quantify the observed loss of membrane connectivity, we analysed the
267 connectivity of all cristae within mitochondrial volumes from different gametocytes (Figure
268 5E-F). We thoroughly searched for crista junctions of each crista found within the
269 mitochondrial segments. Note that these mitochondrial volumes are not full mitochondria,
270 but large segments thereof. As a result of the incompleteness of the mitochondria within the
271 section, and the tomography specific artefact of the missing wedge, we were unable to
272 confirm whether cristae were in fact fully detached from the boundary membrane, or just too
273 long to fit within the observable z-range. Instead, we quantified the fraction of cristae for
274 which we identified a crista junction (Figure 5E). While we identified crista junctions for 55%
275 of the cristae seen in NF54 gametocytes, we could only confirm crista junction presence 9%
276 of the cristae traced in *mic19⁻* and 23% of the cristae in the *mic60⁻* sample. Similarly,
277 connectivity also dropped in the double knockout, with 21% of confirmed crista junctions.
278 Note that for *mic19/60⁻* we chose to measure connectivity in mitochondria that we
279 considered representative for the population average rather than the extreme cases shown
280 in (Figure 4F and Figure S7). For each parasite line, we measured the diameter of at least 12
281 crista junctions and found that this value does not change significantly in the single knockout
282 parasites (Figure 5E-F). Only in *mic19/60⁻* the mean crista junction diameter dropped
283 significantly, from 25 nm in the NF54 control to 20 nm in *mic19/60⁻*. Collectively, these results
284 demonstrate that the deletion of *PfMIC19* and/or *PfMIC60* leads to a reduction of crista
285 junctions

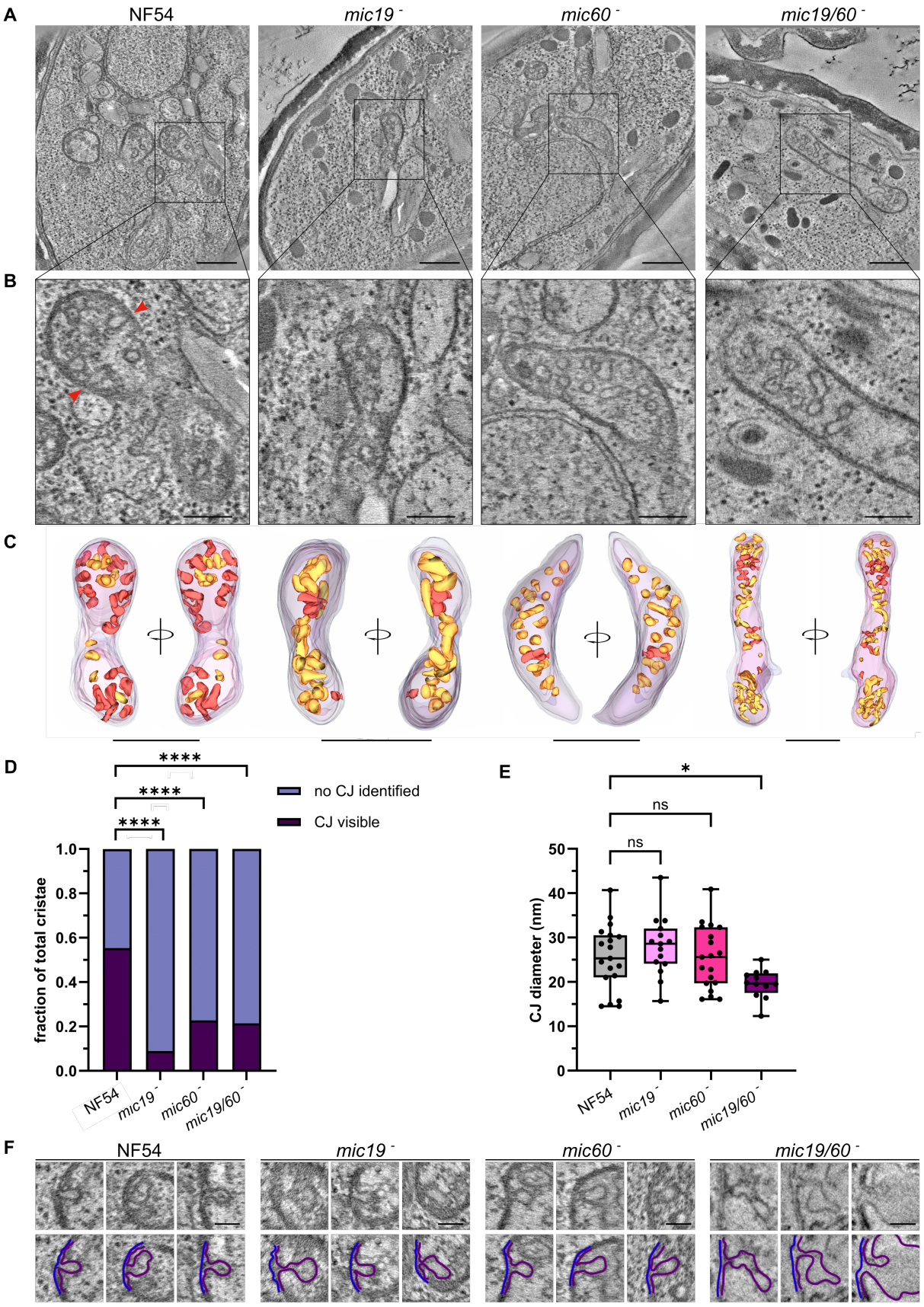

Figure 5. Transmission electron tomography reveals a drop in crista junction prevalence in mature* P. falciparum *mic19⁻, mic60⁻, and mic19/60⁻ gametocytes. *A) Representative snapshots through TEM tomograms of mature NF54 (WT), mic19⁻, mic60⁻, and mic19/mic60⁻ gametocytes. Scale bars: 500 nm. B) Zoom-ins of individual mitochondria from the tomograms shown in A. Crista junctions highlighted*

*with red arrow heads. Scale bars: 200 nm. C) 3D model of 250 nm mitochondrial sections of the mitochondria shown in B. Each model is shown from two angles 180° to each other. Scale bars: 500 nm (full tomograms and mitochondrial segmentations in Movies 1-4). D) Quantification of the relative proportions of cristae for which a crista junction (CJ) was observed within the 250 nm section (n ≥ 56). E) Quantification of the diameter of crista junctions at their narrowest point (n ≥ 12, from several mitochondria per sample). Statistical significance is indicated as follows: ns ≥ 0.05, *p < 0.05, **p < 0.01, ***p < 0.001, ****p < 0.0001. F) Three representative crista junctions from mature NF54, mic19⁻, mic60⁻, and mic19/mic60⁻ gametocytes. Scale bars: 100 nm. 2D segmentation of the outer mitochondrial membrane (blue) and the inner mitochondrial membrane (violet) shown in the bottom row.*

Discussion

MICOS is a protein complex of the inner mitochondrial membrane that is involved in the organization of mitochondrial cristae and stabilization of crista junctions (3-6). Though well established as the cristae organizing system, the role of MICOS in initial formation of cristae remains hidden in model organisms that constitutively display cristae. Currently, *P. falciparum,* the parasite responsible for human malaria, and *Amoebophrya ceratii,* a parasite infecting free-living dinoflagellates, are the only species that reportedly grow cristae *de novo*, from a fully acristate mitochondrion (17, 33). Due to its medical relevance, and the central role of the mitochondria as a validated drug target (34, 35), *P. falciparum* is an invaluable model to study the role of MICOS in cristae organization and formation. Recent bioinformatic data revealed a putative *Pf*MIC60, thus priming the investigation of other components of the complex (9, 16). In this study, we investigated the roles of the putative *PfMIC60* and *PfMIC19* orthologues in cristae formation and organization.

The *P. falciparum* mitochondrial proteome intensely varies between different life cycle stages. In fact, almost all proteins involved in oxidative phosphorylation are dramatically increased in gametocyte stages compared to ABS (36, 37). The same trend was observed for *Pf*MIC19 and *Pf*MIC60. Although transcriptomic data suggested that low-level transcripts of *PfMIC19* and *PfMIC60* are present in ABS (38), we did not detect either of the proteins in ABS by western blot analysis. In contrast, both proteins were detectable, albeit in low abundance, in mature gametocytes. The expression patterns of *Pf*MIC19 and *Pf*MIC60 is consistent with the absence of cristae in ABS and their appearance during gametocytogenesis (17, 37). The low abundance of *Pf*MICOS components even in mature gametocytes likely contributed to our difficulties confirming mitochondrial localization of *Pf*MIC19 and *Pf*MIC60 using fluorescence microscopy.

The absence of *Pf*MIC19 and *Pf*MIC60 during ABS also explains the lack of a growth defect in this part of the life cycle. Surprisingly though, gametocytes and mosquito stages, that are believed to strongly rely on oxidative phosphorylation for their survival (36, 37), were largely unaffected by depletion of these MICOS components, with the exception of a slight reduction in infectivity and oocyst formation. This lack of growth arrest has also been described for the

332 knockout of single MICOS components in human cells, yeast and *Trypanosoma brucei* (11, 39-
333 41). On the other hand, MICOS has been reported to partially impair cell respiration due to
334 mitochondrial disorganization and destabilization of respiratory complexes including ATP
335 synthase (6, 14, 42, 43). Considering these relationships, successful propagation suggests that
336 either the growth defect is masked by the unnaturally rich environment that the parasites
337 encounter in blood culture medium (38), or that the reported impact on respiratory
338 complexes does not occur to a relevant extent in *P. falciparum*.
339
340 Consistent with prior observations in human cells (6, 44), knockouts of *Pf*MIC19 and *Pf*MIC60
341 strongly altered mitochondrial morphology. In fact, both the single and the double knockout
342 parasite lines exhibited mitochondria that were more rounded-up and spherical. The
343 presence of rounded-up mitochondria upon knockout of MICOS components in human cells
344 has been appointed to a secondary defect in mitochondrial fission and increase of reactive
345 oxygen species and hence general mitochondrial stress (45). Given this background and the
346 extreme variability in mitochondrial shape we assume mitochondrial rounding-up in *P.*
347 *falciparum* is also a consequence of mitochondrial stress, due to the loss of *Pf*MIC19 and
348 *Pf*MIC60, rather than a direct involvement of these proteins in mitochondrial shape or fission.
349 Our observation of this mitochondrial rounding-up in the NF54 parental control, could
350 indicate a baseline level of mitochondrial stress in culture conditions. Similarly, we cannot
351 clearly appoint the reduction in oocyst number to a direct response to the loss of *Pf*MIC19
352 and/or *Pf*MIC60, as it could just reflect mitochondrial stress. Still, it is striking that, despite
353 the pronounced morphological phenotype, and the possibly high mitochondrial stress levels,
354 the parasites appeared mostly unaffected in life cycle propagation, raising questions about
355 the functional relevance of mitochondria at these stages.
356
357 The MitochondriaAnalyzer plug-in for ImageJ, used here for the first time on *P. falciparum*
358 samples, proved to be a potent tool to improve bulk quantification of fluorescence
359 microscopy data (31). Of course, it is also important to consider that while fluorescent
360 microscopy is a powerful technique, it cannot reliably determine the number of mitochondria.
361 As shown by TEM data, mitochondria are often located in very close proximity (17, 46), thus
362 the fluorescence-based mitochondrial counts reflect more on whether mitochondria are
363 sufficiently dispersed to be recognized as separate, rather than providing an absolute count.
364 This measurement is interesting nevertheless, as it demonstrates a dispersion of a natively
365 condensed network of tubular mitochondria.
366
367 While the extent of cristae disruptions in *mic19*$^{-}$ and *mic60*$^{-}$ gametocytes was comparable
368 (as shown in thin section TEM and TEM tomography), the double knockout parasites showed
369 stronger morphological defects compared to the single knockouts. In particular, *mic19/60*$^{-}$
370 presented some cases of extremely disrupted mitochondria with the presence of single- or
371 double-membraned circles within the mitochondrial cross-section. Based on this observation,
372 we envision that an excessive elongation of cristae may result in the formation of double-

373 membrane circle. This indicates that in *P. falciparum* the depletion of just one of these
374 proteins does not fully disrupt MICOS function, whereas the absence of both components has
375 a more extensive destabilising effect. Notably, this is different compared to what was
376 observed in human and yeast, where ablation of just MIC60 is sufficient to deplete
377 functionality of the entire MICOS (11, 15), suggesting that *Pf*MIC60 has a less central role in
378 maintaining overall complex integrity. Nevertheless, our results indicate that *Pf*MIC60 and
379 *Pf*MIC19 are both involved in the crista junction stabilization, just like their human and yeast
380 counterparts. The depletion of either or both *P. falciparum* proteins leads to alterations in the
381 organization of cristae membranes but not in the total cristae coverage, thus suggesting that
382 membrane invaginations still arise, but are not properly arranged in these knockout lines. This
383 suggests that MICOS either isn't fully depleted, with yet unidentified components guiding
384 cristae formation, or that the function of MICOS, at least in *P. falciparum*, is restricted to
385 cristae organization, rather than initial cristae formation.
386
387 While MIC60 knockout in human cells showed an almost complete loss of crista junctions (6),
388 none of our knockout lines showed a complete loss of crista junctions. Nevertheless, we did
389 see a decrease in crista junction abundance in all lines, and a significant reduction of crista
390 junction diameter in the double knockout. Interestingly, in both human and yeast cells, crista
391 junctions exhibit diameters ranging from 12 to 40 nm, with an average of 28 nm, which is
392 consistent and comparable with our observation in the parental NF54 gametocytes (47-49).
393 The change in crista junction structure suggests that, at least in *mic19/60*$^{-}$, the remaining
394 crista junctions are affected by the loss of *Pf*MIC60 and *Pf*MIC19. It remains uncertain, though
395 possible, that protein-mediated stabilization is entirely absent in the double knockout. Even
396 without a stabilizing protein component at crista junctions, residual contact sites between the
397 boundary membrane and the cristae membrane are expected, representing remnants of
398 incomplete vesicularization of nascent, yet unstabilized cristae, possibly driven by the
399 membrane bending activity of the ATP synthase. A loss of the entire stabilization machinery
400 at the crista junction would also explain the increased variability of the measurements and
401 the extreme phenotypes observed in this parasite line. Alternatively, remaining cristae
402 junctions could still be maintained through partially redundant, yet undiscovered MICOS
403 proteins. Though not identified in complexomic analysis, it is tempting to speculate about the
404 presence of a cryptic MIC10 sub complex, not recognized due to high divergence, or a hidden
405 apicomplexan-specific subunit, like the ones recently discovered in *T. brucei* (40, 50). Due to
406 low abundance of *Pf*MIC19 and *Pf*MIC60, however, the identification of potential candidates
407 is challenging.
408
409 It is important to note that effects on crista junction structure upon destabilization of the
410 MIC60 subcomplex is a phenomenon described also in yeast and human cells. (6, 13).
411 Previous studies showed that depletion of MIC60 in HeLa cells led to an increase in crista
412 junction diameter, while the depletion of MIC19 did not affect this parameter (11). In contrast
413 to that, destabilization of the MIC60 tetramer in yeast led to a decrease in crista junction

414 diameter (19). Interestingly, our findings do not suggest effects on crista junction diameter
415 for either one of the single knockouts, while the double knockout resulted in a 20% reduction,
416 thus pointing towards, once again, an increasingly unstable complex. The central, tetrameric
417 coiled coil domain of MIC60 has been suggested to define the diameter of the crista junction
418 (13). While not experimentally proven, MICOS induced stabilization of crista junction
419 diameter is a plausible mechanism also for *P. falciparum*. In fact, the mean diameter of *P.*
420 *falciparum* crista junctions aligns well with the theoretical length of the coiled coil domain
421 predicted by AlphaFold. How this assembly aligns with the phenotypes indicative for partial
422 redundancy with MIC19, however, remains to be investigated.
423
424 Collectively, we have demonstrated that *Pf*MIC19 and *Pf*MIC60 are putative mitochondrial
425 proteins expressed in gametocytes. Their deletion does not affect ABS nor sexual blood stages
426 in standard culture conditions. While oocyst counts were modestly reduced, sporozoite
427 production did not appear to be affected, indicating that the proteins are not essential at any
428 point of the parasite life cycle investigated in this study. Still, knockout of *Pf*MIC19 and
429 *Pf*MIC60 strongly altered mitochondrial morphology in gametocytes, and mitochondrial
430 cristae are aberrant but present, with a reduction in crista junction abundance, confirming a
431 role of these proteins in the *Pf*MICOS. Although molecular mechanisms of membrane bending
432 and anchoring are yet to be elucidated, our study demonstrated the existence of the *Pf*MICOS.
433 In contrast to other systems where MICOS has been described, *P. falciparum* further allows
434 us to clearly decipher cause-effect relationships in this context, as we can conclude that even
435 in the absence of *Pf*MIC60 and *Pf*MIC19, cristae are formed *de novo*, and they allow for
436 parasite survival. Thus, our data provide direct evidence that components of the *Pf*MICOS are
437 essential for crista junction organization and stabilization, but not for initial cristae formation.
438 This functional separation is likely to generalize beyond *P. falciparum*, to evolutionary distant
439 organisms such as human and yeast. Our results highlight the unique utility that the two-state
440 mitochondrial architecture in *P. falciparum* provides to the field of mitochondrial biology and
441 lays the groundwork for future studies on the causal dissection of cristae biogenesis in *P.*
442 *falciparum* gametocytes and beyond.
443

444 Material and Methods

445
446 **Plasmid generation.**
447 To generate the *mic19-HA* and *mic60-HA* homology-direct repair (HDR) plasmids, the pRF0139
448 empty tagging plasmid was used, containing 3xHA-GlmS, PBANKA_142660 bidirectional 3'UTR,
449 and the mitochondrial-mScarlet marker (26). 5' and 3' homology arms (HRs) were amplified
450 from genomic NF54 DNA and cloned specific restriction enzymes (Table S1).
451 HDR templated for *mic19*$^{-}$ and *mic60*$^{-}$ were generated from pGK backbone (51), which
452 contains a pBAT backbone (52) with H2B promotor, GFP and PBANKA_142660 bidirectional

453 3'UTR. The 5' and 3' HRs, amplified from NF54 gDNA, were cloned into pGK using specific
454 restriction sites (Table S1).
455 To generate the HDR template for the *mic19/60*$^{-}$, 5' and 3' HR were inserted into pCK2a, which
456 contains a pBAT backbone (52) with H2B promotor, mCherry and PBANKA_142660
457 bidirectional 3'UTR.
458 Cas9 guide plasmids were generated inserting a pair of annealed complementary, guide
459 encoding, oligonucleotides into pBF-gC (53) or, a derived plasmid from MLB626 (54) (kind gift
460 from Marcus Lee) that does not present an 3xHA tag in the Cas9 gene. BsaI and BbsI,
461 respectively, restriction enzymes were used to insert the oligonucleotides and generate the
462 final guide plasmids (Table S1). All PCR reactions were performed using Primestar GXL DNA
463 polymerase (Takara Bio), and all cloning enzymes were obtained via New England Biolabs.
464
465 ***P. falciparum* culturing and transfection.** *P. falciparum* asexual blood-stage parasites were
466 cultured in complete RPMI medium (with 25 mM HEPES, 100 mM hypoxanthine, and 24 mM
467 sodium bicarbonate) supplemented with 10% AB+ human serum and 5% 0+ human Red Blood
468 Cells (RBCs) (Sanquin, The Netherlands) (55). The cultures were kept at 37° C in a low oxygen
469 environment (3% O_2, 4% CO_2). When needed, ring parasites synchronization was achieved
470 using sorbitol treatment (56). Culture parasitaemia, was monitored with Giemsa-stained
471 blood smears using a 100X oil objective.
472
473 For transfections 60 µg of each Cas9 guides and linearized repair plasmids were ethanol
474 precipitated and transfected on a ring-stage synchronized culture, as previously described
475 (57). Briefly, the plasmids were dissolved and mixed with cytomix (0.895% KCl, 0.0017% $CaCl_2$,
476 0.076% EGTA, 0.102% $MgCl_2$, 0.0871% K_2HPO_4, 0.068% KH_2PO_4, 0.708% HEPES) for a total
477 volume of 300 µl. The DNA was then added to 0.4 ml of packed ring-stage infected RBCs and
478 the solution was electroporated (0.31 kV and 950 uF). Parasites were left to recover for 4 h
479 after transfection in complete media and after that treated in 2.5 nM WR99210 (Jacobus
480 Pharmaceuticals) or 40 µg/ml blasticidin (Gibco #R210-01) for 5 days. To obtain an isogenic
481 population, parasites were isolated using flow cytometry (58) based on GFP (*mic19*$^{-}$ and
482 *mic60*$^{-}$), mCherry (*mic19/60*$^{-}$) or mScarlet (*mic19-HA* and *mic60-HA*) expression, using a
483 CytoFLEX SRT benchtop Cell Sorter (Beckman Coulter). Transfected parasites were cultured
484 until recovered and integration was confirmed by diagnostic PCR (Table S1).
485
486 **Growth assay.** Parasite cultures were tightly synchronized through a double sorbitol
487 synchronisation performed at 0 h and 16 h. Ring-stage parasites were determined through
488 flow cytometry and cultures were diluted to have a 0.5% final parasitaemia. Cultures were set
489 up at 0.5% parasitaemia and samples were harvested for 4 days. Samples for flow cytometry
490 were taken directly after set-up, on day 1, 2 before and after dilution, 3 and 4. On day 2 all
491 cultures were diluted with the same dilution factor (1/20). When harvested, samples were
492 fixed in 0.25% glutaraldehyde (ITW Reagents, CA0589.100) in PBS and, before flow cytometry

493 (Cytoflex - 13-color, Beckman Coulter), stained with SYBR™ green (ThermoFisher, 7563)
494 1:10.000 for 30 min at 37° C. Data was analysed using FlowJo software (version 10.10).
495
496 **Gametocyte culture conditions and standard membrane feeding assay.** Sexual conversion in
497 parasites was induced in a trophozoite-stage culture, adding Albumax- containing medium for
498 36 h and changed every 12 h (59). Gametocytes were then cultured with normal culture
499 medium until maturation. During the entire procedure gametocytes were kept at 37° C in low
500 oxygen conditions. To remove ABS from culture, gametocytes were cultured with heparin (20
501 U/ml) for 4 days. To quantify exflagellation, cultures were mixed 1:1 with 50 µM xanthurenic
502 acid in complete RPMI medium. The solution, kept at room temperature for 15 min, was then
503 transferred to a Neubauer chamber where the exflagellation centres were counted with a 40X
504 objective by bright-field microscopy. To assess mosquito infectivity, day 12 mature
505 gametocytes (59) were added to the bloodmeal of *Anopheles stephensi* mosquitoes (colony
506 maintained at Radboudumc, Nijmegen, The Netherlands), as previously described (60). Mean
507 oocysts per midgut and statistical significance were calculated using a generalized linear
508 mixed effect model with a random experiment effect under a negative binomial distribution.
509
510 **Fluorescence microscopy.** Mature gametocytes were incubated in 100 nM MitoTracker
511 (MitoTracker® Orange CMTMRos, Thermo Fisher, #M7510) diluted in incomplete medium for
512 exactly 30 min at 37° C and afterwards washed and diluted 1:10 in incomplete medium. The
513 samples were allowed to settle on poly-L-Lysin coverslips (Corning, #354085) for 30 min at 37°
514 C before being fixed in 4% paraformaldehyde (Thermo Fisher, #28906) and 0.0075%
515 glutaraldehyde (Panreac, #A0589,0010) in PBS for 20 min (61). The samples were then
516 washed with 1X PBS and permeabilized with 0.1% Triton X-100 in PBS for 10 min. Cells were
517 blocked with 3% BSA for 1 h at RT. The coverslips were incubated with primary antibodies
518 diluted in PBS with 3% BSA (Table S2) for 1 h at RT, washed three times and then incubated
519 with the secondary antibodies again for 1 h at RT. All the samples were additionally stained
520 with 300 nM DAPI (Thermo Fisher, #62248) for 1 h before being mounted onto microscope
521 slides with Fluoromount G (Thermo Fisher, # 00-4958-02). Images were acquired using an
522 LSM900 confocal microscope with airyscan (ZEISS) using a 63x oil objective with 405, 488, 561,
523 and 633 nm laser excitation and an Electronically Switchable Illumination and Detection
524 Model (ESID) for transmitted light. Images belonging to the same experiment were acquired
525 with equal setting for laser power and detector sensibility and afterwards analyzed with the
526 same parameters to compare expression.
527
528 **Mitochondria quantification in fluorescence microscopy.** Mature gametocytes prepared as
529 previously explained, were randomly selected based on DIC or DAPI signal to avoid bias.
530 Mitochondria were quantified using the Fiji plug-in MitochondriaAnalyser (31). Briefly, 3D
531 image stacks were pre-processed using the following commands: subtract background
532 (radius = 1.25 µm); sigma filter plus (radius = 2.0 µm); enhance local contrast (slope = 1.40
533 µm); and gamma correction (value = 0.9 µm). For thresholding, block size was set to 0.85 µm

534 with a C value of 7. Thresholded images were then postprocessed using the functions
535 despeckle and remove outliers with radius = 3 pixels. Statistical significance was determined
536 using one-way ANOVA test with Sidàk correction. Mitochondria were divided in tubular,
537 intermediate and round up based on average branch length (total branch length / number of
538 mitochondria intensities) and statistical significance was determined using a chi-squared test.
539
540 **Ultra-Expansion Microscopy (U-ExM).** Mature gametocytes were isolated using MACS LS
541 columns. Shortly, LS columns were equilibrated using incomplete media and mature
542 gametocyte cultures were flushed in the LS columns attached to a magnet using a 23G needle
543 to regulate the flow. To elute gametocytes, columns were removed from the magnet and
544 washed with incomplete media. MACS column, magnet and incomplete media were
545 previously incubated at 37° C, and kept in temperature for all procedure, to prevent
546 gametocytes activation during purification. The gametocytes pellet was then incubated with
547 100 nM MitoTracker and fixed as previously explained. The coverslips were then incubated
548 with 0.5% acrylamide (AA) (Sigma, #A4058) and 0.38% formaldehyde (FA) (Sigma, #F8775) in
549 PBS overnight at 37° C. Gelation was performed as previously described (62). Briefly the
550 gelling solution was prepared adding tetramethylethylenediamine (TMED, final concentration
551 0.5%) (Sigma, #T7024) and ammonium persulfate (APS, final concentration 0.5%) (Sigma,
552 #A3678) to U-ExM monomer solution (MS) (23% w/v sodium acrylate (AK Scientific, #R624),
553 10% w/v AA, N,N'-methylenbisacrylamide (BIS) (Sigma, #M1533) 0.1% w/v in PBS). The
554 solution was then added to the coverslips and incubated at 37° C for 1 h. Gels were incubated
555 with denaturation buffer (200 mM SDS, 200 mM NaCl, 50 mM Tris in water, pH 9) under strong
556 agitation until complete detachment from the coverslips and transferred into a 1.5 ml
557 Eppendorf tube filled with denaturation buffer and incubated 90 minutes at 95° C. Gels were
558 expanded overnight in MQ at RT. Following, gels were incubated with primary antibodies
559 (Table S2) for 3 h at 37° C while shaking, followed by secondary antibodies, NHS-ester (8 µg/ml)
560 (DyLightTM 405 NHS-ester, ThermoScientific, #46400) and SYTOX^{TM} (Thermo Fisher, #S11381)
561 for 2.5 h at 37° C, shaking. For imaging, gels were cut into pieces and positioned on a poly-D
562 lysine (Gibco, #A38904-01) coated coverslip. Images were acquired with identical parameters,
563 using an LSM900 confocal microscope with airyscan (ZEISS) using a 63X oil objective with 405,
564 488, 561, and 633 nm laser excitation and an Electronically Switchable Illumination and
565 Detection Model (ESID) for transmitted light.
566
567 **Electron microscopy sample preparation.** Mature gametocytes were harvested using MACS
568 LS columns as previously explained. Purified gametocytes were then fixed with 4% PFA in 0.1
569 M PHEM and pelleted at 600 x g for 10 min. The pellets were vitrified using the Leica EMPACT
570 high pressure freezer with membrane carrier assembly. Water removal and staining was
571 achieved by freeze substitution in 1% osmium tetroxide, 0.2% uranyl acetate and 1% water in
572 acetone. Stepwise freeze substitution consisted of a 48 h incubation at -90° C, temperature
573 sloped increase to -60° C within 12 h, 10 h incubation at -60° C, sloped increase to -60° C
574 within 12 h, incubation at -30° C for 8 h and removal of uranyl acetate by washing in 1%

575 osmium tetroxide in acetone at -30° C. The samples were then transferred to ice, osmium
576 tetroxide was replaced with pure acetone, and the samples were further stained with 1%
577 tannic acid in acetone for 1 h and with 1% osmium tetroxide for 1 h. Then the samples were
578 embedded in Epon (46% HY 964 Araldite, 39.6% Epoxy Embedding Medium, 13% MNA, 1.4%
579 DMP-30) in a stepwise increase of the Epon to acetone ratio. Fully infiltrated samples were
580 hardened at 70° C for 5 days. Thin sections of 65 nm or semi-thin sections of 250 nm were
581 collected on copper grids with formvar/carbon coating. Thin sections were post stained with
582 2% uranyl acetate for 2 min and Reynolds lead citrate (Reynolds, 1963) for 5 min. Semi-thin
583 sections were labelled with 15 nm gold fiducials for tilt-series alignment.
584
585 **Transmission electron tomography.** All tomograms were recorded at a JEOL2100 TEM
586 operating at 200 kV. Tomograms were recorded as dual-axis tilt series at 1.5° increment at a
587 range of -60° to 60° (pixel size 1.52 nm, defocus –1.1 µm). Reconstruction, segmentation and
588 quantifications were performed manually, in IMOD. The statistical significance of the
589 deviations in crista junction diameter was determined using one-way ANOVA test with Sidàk
590 correction. Significance of the difference in crista junction prevalence was tested using a Chi-
591 squared test.
592
593 **Thin section electron microscopy.** Micrographs were collected at a JEOL1400 TEM operating
594 at 120 kV. Recorded images were randomized for blinded quantification of cristae length,
595 diameter, area, and coverage. Statistical significance was determined using one-way ANOVA
596 tests with Sidàk correction.
597
598 **SDS-Page gel and western blot.** Saponin pellet of gametocytes and asexual blood-stage
599 cultures were prepared by resuspending in 7X pellet volume MQ and 2X pellet volume
600 reductive loading buffer (1% β-mercaptoethanol, 0.004% bromophenol blue, 6% glycerol, 2%
601 SDS 50 mM Tris-HCl, pH 6.8). Samples were heated at 70° C for 10 min, quickly vortexed and
602 spun down to precipitate insoluble debris and DNA. The supernatant was loaded on a
603 SurePAGE, 8% Bis-Tris SDS-PAGE (GenScript, #M00677). A standard protein ladder (Precision
604 Plus Protein in Dual Colour Standard, Bio-Rad) was included in every run. Proteins were
605 transferred, with the semi-wet transfer method, to a nitrocellulose membrane soaked in
606 transfer buffer (20% methanol with 10% Tris-Glycine (10X)) in a Trans-Blot Turbo machine
607 (Bio-Rad) at 25V for 30 min. The membrane was then blocked in 1% milk powder in PBS with
608 0.05% Tween 20 (PBST) overnight at 4° C. Primary and secondary antibodies (Table S2) were
609 diluted in 1% milk powder in PBST and incubated for 1 h at RT. The blot was then imaged with
610 Odyssey CLx (ImageQuant).
611
612 **Structural comparisons and domain predictions.** All AlphaFold models were retrieved from
613 the AlphaFold protein structure database (ScMIC60: AF-P36112-F1-v4, *Pf*MIC60: AF-. Q8IJW5-
614 F1-v4, ScMIC19: AF-P43594-F1-v4, *Pf*MIC19: AF-Q8IIR5-F1-v4)(27, 28). Domains were used as
615 predicted by TED consensus domain, retrieved from the AlphaFold protein structure database

616 (29). Associated pLDDT prediction confidence information is shown in Figure S1. Theoretical
617 length of the coiled coil domain in ScMIC60 and *Pf*MIC60 was measured by atomic distance
618 within the predicted models.
619

620 ACKNOWLEDGEMENTS

621 We would like to thank all members of the molecular & cellular parasitology team at the
622 Radboudumc and the microbiology department at the Radboud University for the discussion
623 and support during the project. We would like to thank the General Instrumentation
624 Department at Radboud University, Radboud Technology Center Microscopy and the
625 Radboud Technology Center Flowcytometry for use of their microscopy and flow cytometry
626 facilities. In addition, we also thank Jordache Ramjith for his advice and support in the
627 statistical analysis. This work was supported by funding provided by the Dutch Research
628 Council (NWO, grant number: OCENW.M.21.087) awarded to Taco W.A. Kooij and Laura van
629 Niftrik. **Author contributions:** LvN and TWAK obtained funding and conceptualized and
630 supervised the project; STL, IB and JLO performed experiments; STL, IB, JLO, FE, TWAK and
631 LvN analysed data; NIP, GJvG and RS executed the mosquito experiments; STL and IB wrote
632 the first draft of the manuscript and all authors reviewed, edited and approved the
633 manuscript.
634

635 REFERENCES

636 1. Wurm CA, Jakobs S. Differential protein distributions define two sub-compartments
637 of the mitochondrial inner membrane in yeast. FEBS Lett. 2006;580(24):5628-34.
638 2. Gilkerson RW, Selker JM, Capaldi RA. The cristal membrane of mitochondria is the
639 principal site of oxidative phosphorylation. FEBS Lett. 2003;546(2-3):355-8.
640 3. Vogel F, Bornhovd C, Neupert W, Reichert AS. Dynamic subcompartmentalization of
641 the mitochondrial inner membrane. J Cell Biol. 2006;175(2):237-47.
642 4. Frey TG, Renken CW, Perkins GA. Insight into mitochondrial structure and function
643 from electron tomography. Biochim Biophys Acta. 2002;1555(1-3):196-203.
644 5. van der Laan M, Horvath SE, Pfanner N. Mitochondrial contact site and cristae
645 organizing system. Curr Opin Cell Biol. 2016;41:33-42.
646 6. Stephan T, Bruser C, Deckers M, Steyer AM, Balzarotti F, Barbot M, et al. MICOS
647 assembly controls mitochondrial inner membrane remodeling and crista junction
648 redistribution to mediate cristae formation. EMBO J. 2020;39(14):e104105.
649 7. Harner M, Korner C, Walther D, Mokranjac D, Kaesmacher J, Welsch U, et al. The
650 mitochondrial contact site complex, a determinant of mitochondrial architecture. EMBO J.
651 2011;30(21):4356-70.
652 8. von der Malsburg K, Muller JM, Bohnert M, Oeljeklaus S, Kwiatkowska P, Becker T, et
653 al. Dual role of mitofilin in mitochondrial membrane organization and protein biogenesis.
654 Dev Cell. 2011;21(4):694-707.
655 9. Huynen MA, Muhlmeister M, Gotthardt K, Guerrero-Castillo S, Brandt U. Evolution
656 and structural organization of the mitochondrial contact site (MICOS) complex and the

657 mitochondrial intermembrane space bridging (MIB) complex. Biochim Biophys Acta.
658 2016;1863(1):91-101.
659 10. Zerbes RM, Bohnert M, Stroud DA, von der Malsburg K, Kram A, Oeljeklaus S, et al.
660 Role of MINOS in mitochondrial membrane architecture: cristae morphology and outer
661 membrane interactions differentially depend on mitofilin domains. J Mol Biol.
662 2012;422(2):183-91.
663 11. Friedman JR, Mourier A, Yamada J, McCaffery JM, Nunnari J. MICOS coordinates with
664 respiratory complexes and lipids to establish mitochondrial inner membrane architecture.
665 Elife. 2015;4.
666 12. Barbot M, Jans DC, Schulz C, Denkert N, Kroppen B, Hoppert M, et al. Mic10
667 oligomerizes to bend mitochondrial inner membranes at cristae junctions. Cell Metab.
668 2015;21(5):756-63.
669 13. Bock-Bierbaum T, Funck K, Wollweber F, Lisicki E, von der Malsburg K, von der
670 Malsburg A, et al. Structural insights into crista junction formation by the Mic60-Mic19
671 complex. Sci Adv. 2022;8(35):eabo4946.
672 14. Rabl R, Soubannier V, Scholz R, Vogel F, Mendl N, Vasiljev-Neumeyer A, et al.
673 Formation of cristae and crista junctions in mitochondria depends on antagonism between
674 Fcj1 and Su e/g. J Cell Biol. 2009;185(6):1047-63.
675 15. Korner C, Barrera M, Dukanovic J, Eydt K, Harner M, Rabl R, et al. The C-terminal
676 domain of Fcj1 is required for formation of crista junctions and interacts with the TOB/SAM
677 complex in mitochondria. Mol Biol Cell. 2012;23(11):2143-55.
678 16. Evers F, Cabrera-Orefice A, Elurbe DM, Kea-Te Lindert M, Boltryk SD, Voss TS, et al.
679 Composition and stage dynamics of mitochondrial complexes in Plasmodium falciparum. Nat
680 Commun. 2021;12(1):3820.
681 17. Evers F, Roverts R, Boshoven C, Kea-Te Lindert M, Verhoef JMJ, Sommerdijk N, et al.
682 Comparative 3D ultrastructure of Plasmodium falciparum gametocytes. Nat Commun.
683 2025;16(1):69.
684 18. Ke H, Lewis IA, Morrisey JM, McLean KJ, Ganesan SM, Painter HJ, et al. Genetic
685 investigation of tricarboxylic acid metabolism during the Plasmodium falciparum life cycle.
686 Cell Rep. 2015;11(1):164-74.
687 19. MacRae JI, Dixon MW, Dearnley MK, Chua HH, Chambers JM, Kenny S, et al.
688 Mitochondrial metabolism of sexual and asexual blood stages of the malaria parasite
689 Plasmodium falciparum. BMC Biol. 2013;11:67.
690 20. Srivastava A, Philip N, Hughes KR, Georgiou K, MacRae JI, Barrett MP, et al. Stage-
691 Specific Changes in Plasmodium Metabolism Required for Differentiation and Adaptation to
692 Different Host and Vector Environments. PLoS Pathog. 2016;12(12):e1006094.
693 21. Sheokand PK, Pradhan S, Maclean AE, Muhleip A, Sheiner L. Plasmodium falciparum
694 Mitochondrial Complex III, the Target of Atovaquone, Is Essential for Progression to the
695 Transmissible Sexual Stages. Int J Mol Sci. 2024;25(17).
696 22. Muhleip A, Kock Flygaard R, Ovciarikova J, Lacombe A, Fernandes P, Sheiner L,
697 Amunts A. ATP synthase hexamer assemblies shape cristae of Toxoplasma mitochondria. Nat
698 Commun. 2021;12(1):120.
699 23. Munoz-Gomez SA, Slamovits CH, Dacks JB, Wideman JG. The evolution of MICOS:
700 Ancestral and derived functions and interactions. Commun Integr Biol. 2015;8(6):e1094593.
701 24. Perkins G, Renken C, Martone ME, Young SJ, Ellisman M, Frey T. Electron tomography
702 of neuronal mitochondria: three-dimensional structure and organization of cristae and
703 membrane contacts. J Struct Biol. 1997;119(3):260-72.

25. Chen F, Mackey AJ, Stoeckert CJ, Jr., Roos DS. OrthoMCL-DB: querying a comprehensive multi-species collection of ortholog groups. Nucleic Acids Res. 2006;34(Database issue):D363-8.
26. Verhoef JMJ, Boshoven C, Evers F, Akkerman LJ, Gijsbrechts BCA, van de Vegte-Bolmer M, et al. Detailing organelle division and segregation in Plasmodium falciparum. J Cell Biol. 2024;223(12).
27. Jumper J, Evans R, Pritzel A, Green T, Figurnov M, Ronneberger O, et al. Highly accurate protein structure prediction with AlphaFold. Nature. 2021;596(7873):583-9.
28. Varadi M, Anyango S, Deshpande M, Nair S, Natassia C, Yordanova G, et al. AlphaFold Protein Structure Database: massively expanding the structural coverage of protein-sequence space with high-accuracy models. Nucleic Acids Res. 2022;50(D1):D439-D44.
29. Lau AM, Bordin N, Kandathil SM, Sillitoe I, Waman VP, Wells J, et al. Exploring structural diversity across the protein universe with The Encyclopedia of Domains. Science. 2024;386(6721):eadq4946.
30. Rawlings DJ, Fujioka H, Fried M, Keister DB, Aikawa M, Kaslow DC. Alpha-tubulin II is a male-specific protein in Plasmodium falciparum. Mol Biochem Parasitol. 1992;56(2):239-50.
31. Chaudhry A, Shi R, Luciani DS. A pipeline for multidimensional confocal analysis of mitochondrial morphology, function, and dynamics in pancreatic beta-cells. Am J Physiol Endocrinol Metab. 2020;318(2):E87-E101.
32. Schindelin J, Arganda-Carreras I, Frise E, Kaynig V, Longair M, Pietzsch T, et al. Fiji: an open-source platform for biological-image analysis. Nat Methods. 2012;9(7):676-82.
33. Decelle J, Kayal E, Bigeard E, Gallet B, Bougoure J, Clode P, et al. Intracellular development and impact of a marine eukaryotic parasite on its zombified microalgal host. The ISME Journal. 2022;16(10):2348-59.
34. Gujjar R, Marwaha A, El Mazouni F, White J, White KL, Creason S, et al. Identification of a metabolically stable triazolopyrimidine-based dihydroorotate dehydrogenase inhibitor with antimalarial activity in mice. J Med Chem. 2009;52(7):1864-72.
35. Goodman CD, Buchanan HD, McFadden GI. Is the Mitochondrion a Good Malaria Drug Target? Trends in Parasitology. 2017;33(3):185-93.
36. Sparkes PC, Famodimu MT, Alves E, Springer E, Przyborski J, Delves MJ. Mitochondrial ATP synthesis is essential for efficient gametogenesis in Plasmodium falciparum. Commun Biol. 2024;7(1):1525.
37. Sturm A, Mollard V, Cozijnsen A, Goodman CD, McFadden GI. Mitochondrial ATP synthase is dispensable in blood-stage Plasmodium berghei rodent malaria but essential in the mosquito phase. Proc Natl Acad Sci U S A. 2015;112(33):10216-23.
38. Kubihal S, Goyal A, Gupta Y, Khadgawat R. Glucose measurement in body fluids: A ready reckoner for clinicians. Diabetes Metab Syndr. 2021;15(1):45-53.
39. Weber TA, Koob S, Heide H, Wittig I, Head B, van der Bliek A, et al. APOOL is a cardiolipin-binding constituent of the Mitofilin/MINOS protein complex determining cristae morphology in mammalian mitochondria. PLoS One. 2013;8(5):e63683.
40. Kaurov I, Vancova M, Schimanski B, Cadena LR, Heller J, Bily T, et al. The Diverged Trypanosome MICOS Complex as a Hub for Mitochondrial Cristae Shaping and Protein Import. Curr Biol. 2018;28(21):3393-407 e5.
41. Kondadi AK, Anand R, Hansch S, Urbach J, Zobel T, Wolf DM, et al. Cristae undergo continuous cycles of membrane remodelling in a MICOS-dependent manner. EMBO Rep. 2020;21(3):e49776.

42. Rampelt H, Wollweber F, Licheva M, de Boer R, Perschil I, Steidle L, et al. Dual role of Mic10 in mitochondrial cristae organization and ATP synthase-linked metabolic adaptation and respiratory growth. Cell Rep. 2022;38(4):110290.
43. Cadena LR, Gahura O, Panicucci B, Zikova A, Hashimi H. Mitochondrial Contact Site and Cristae Organization System and F(1)F(O)-ATP Synthase Crosstalk Is a Fundamental Property of Mitochondrial Cristae. mSphere. 2021;6(3):e0032721.
44. Benning FMC, Bell TA, Nguyen TH, Syau D, Connell LB, Liao YT, et al. Ancestral sequence reconstruction of the Mic60 Mitofilin domain reveals residues supporting respiration in yeast. bioRxiv. 2025.
45. Genin EC, Plutino M, Bannwarth S, Villa E, Cisneros-Barroso E, Roy M, et al. CHCHD10 mutations promote loss of mitochondrial cristae junctions with impaired mitochondrial genome maintenance and inhibition of apoptosis. EMBO Mol Med. 2016;8(1):58-72.
46. Okamoto N, Spurck TP, Goodman CD, McFadden GI. Apicoplast and mitochondrion in gametocytogenesis of Plasmodium falciparum. Eukaryot Cell. 2009;8(1):128-32.
47. Frey TG, Mannella CA. The internal structure of mitochondria. Trends in Biochemical Sciences. 2000;25(7):319-24.
48. Nicastro D, Frangakis AS, Typke D, Baumeister W. Cryo-electron tomography of neurospora mitochondria. J Struct Biol. 2000;129(1):48-56.
49. Perkins GA, Ellisman MH, Fox DA. Three-dimensional analysis of mouse rod and cone mitochondrial cristae architecture: bioenergetic and functional implications. Mol Vis. 2003;9:60-73.
50. Eichenberger C, Oeljeklaus S, Bruggisser J, Mani J, Haenni B, Kaurov I, et al. The highly diverged trypanosomal MICOS complex is organized in a nonessential integral membrane and an essential peripheral module. Mol Microbiol. 2019;112(6):1731-43.
51. Verhoef JMJ, Bekkering ET, Boshoven C, Hannon M, Proellochs NI, Spruijt CG, Kooij TWA. The role of stomatin-like protein (STOML) in Plasmodium falciparum. bioRxiv. 2024:2024.07.18.604071.
52. Kooij TW, Rauch MM, Matuschewski K. Expansion of experimental genetics approaches for Plasmodium berghei with versatile transfection vectors. Mol Biochem Parasitol. 2012;185(1):19-26.
53. Filarsky M, Fraschka SA, Niederwieser I, Brancucci NMB, Carrington E, Carrio E, et al. GDV1 induces sexual commitment of malaria parasites by antagonizing HP1-dependent gene silencing. Science. 2018;359(6381):1259-63.
54. Lim MY, LaMonte G, Lee MCS, Reimer C, Tan BH, Corey V, et al. UDP-galactose and acetyl-CoA transporters as Plasmodium multidrug resistance genes. Nat Microbiol. 2016;1:16166.
55. Trager W, Jensen JB. Human malaria parasites in continuous culture. Science. 1976;193(4254):673-5.
56. Lambros C, Vanderberg JP. Synchronization of Plasmodium falciparum Erythrocytic Stages in Culture. The Journal of Parasitology. 1979;65(3):418-20.
57. Wu Y, Sifri CD, Lei HH, Su XZ, Wellems TE. Transfection of Plasmodium falciparum within human red blood cells. Proc Natl Acad Sci U S A. 1995;92(4):973-7.
58. Kenthirapalan S, Waters AP, Matuschewski K, Kooij TW. Flow cytometry-assisted rapid isolation of recombinant Plasmodium berghei parasites exemplified by functional analysis of aquaglyceroporin. Int J Parasitol. 2012;42(13-14):1185-92.

796 59. Graumans W, van der Starre A, Stoter R, van Gemert GJ, Andolina C, Ramjith J, et al.
797 AlbuMAX supplemented media induces the formation of transmission-competent P.
798 falciparum gametocytes. Mol Biochem Parasitol. 2024;259:111634.
799 60. Stone WJ, Eldering M, van Gemert GJ, Lanke KH, Grignard L, van de Vegte-Bolmer
800 MG, et al. The relevance and applicability of oocyst prevalence as a read-out for mosquito
801 feeding assays. Sci Rep. 2013;3:3418.
802 61. Tonkin CJ, van Dooren GG, Spurck TP, Struck NS, Good RT, Handman E, et al.
803 Localization of organellar proteins in Plasmodium falciparum using a novel set of
804 transfection vectors and a new immunofluorescence fixation method. Mol Biochem
805 Parasitol. 2004;137(1):13-21.
806 62. Gambarotto D, Hamel V, Guichard P. Ultrastructure expansion microscopy (U-ExM).
807 Methods Cell Biol. 2021;161:57-81.
808